PHYSICAL REVIEW B **98**, 035417 (2018)

Spectroscopic properties of a freestanding $MnPS_3$ single layer

M. K. Kinyanjui,[1] J. Koester,[1] F. Boucher,[2] A. Wildes,[3] and U. Kaiser[1]
[1] *Central Facility of Electron Microscopy, Ulm University, Ulm, Germany*
[2] *Institut des Matériaux Jean Rouxel (IMN), Université de Nantes, CNRS, 2 rue de la Houssinière, BP 32229, 44322 Nantes Cedex 3, France*
[3] *Institut Laue-Langevin, CS 20156, 388042 Grenoble Cedex 9, France*

(Received 8 December 2017; revised manuscript received 11 May 2018; published 10 July 2018)

Quasi-two-dimensional manganese thiophosphate, $MnPS_3$, is interesting due to its two-dimensional antiferromagnetic structure observed at low temperatures as well as possible technological applications. While the spectroscopic properties of bulk $MnPS_3$ structures have been extensively studied, the spectroscopic characteristics of freestanding $MnPS_3$ layers are yet to be explored. We present an experimental study on the spectroscopic properties of a freestanding $MnPS_3$ single layer obtained through exfoliation from bulk $MnPS_3$. We find that the position of the main peak in the electron-energy-loss spectrum (EELS) is shifted from approximately 19 eV in bulk $MnPS_3$ to 15 eV in single $MnPS_3$ layer. Theoretical calculations show that this peak corresponds to a volume plasmon in bulk $MnPS_3$ and a damped plasmon peak in single-layer $MnPS_3$. In addition, the dispersion of this peak was investigated using momentum-resolved electron-energy-loss spectroscopy. The peak dispersion for the single-layer $MnPS_3$ displays a square-root behavior characteristic of a two-dimensional plasmon. We show that EELS spectra provide both a means to identify single-layer $MnPS_3$ from bulk structures and also show the effects of low dimensionality on the electronic excitations.

DOI: 10.1103/PhysRevB.98.035417

I. INTRODUCTION

Transition-metal thiophosphates (MPX_3) are layered structures where a $3d$ transition metal (M) is bonded to phosphorous (P) and chalcogen atoms ($X =$ S, Se) [1,2]. Bulk MPX_3 structures are usually Mott insulators which also show antiferromagnetic (AFM) ordering at low temperatures [3–5]. The bulk structure of MPX_3 layers can be described using (1) an ionic model where high-spin M^{2+} cations are bonded to anionic $[P_2X_6]^{4-}$ clusters; (2) an MX_2 model similar to transition-metal dichalcogenides where a third of the cation (M) sites are substituted by a pair of phosphorous atoms, giving $M_{2/3}(P_2)_{1/3}S_2$ [1]. Individual MPX_3 layers are bonded through weak van der Waals (vdW) interactions. The structure of bulk $MnPS_3$ is shown in Fig. 1, where a single $MnPS_3$ layer ($Mn_2P_2S_6$ slab) and the vdW gap between individual $MnPS_3$ layers are indicated [1].

Due to their layered nature, MPX_3 structures can be intercalated with metal ions and organic molecules [6]. The intercalation of the molecules and ions takes place within the vdW gap and is also associated with charge transfer from the intercalate to the host structure [6–8]. The weak vdW bonding interaction between individual MPX_3 layers makes it possible to isolate single MPX_3 layers using either chemical or mechanical exfoliation [9–16]. The obtained single MPX_3 layers are unique since they are insulators and are also characterized by AFM magnetic ordering not observed in graphene or transition-metal dichalcogenides single layers [13,14].

Understanding the electronic structure of such single layers is therefore of great interest both for fundamental solid-state research and potential applications [9]. It is especially important to understand how the spectroscopic properties of single freestanding layers differ from bulk structures [10,15]. This includes, among others, understanding the nature of various electronic excitations such as excitons and plasmons in freestanding single layers. Spectroscopic properties of bulk MPX_3 structures have been well studied [17–23]. On the other hand, the spectroscopic properties of freestanding MPX_3 layers have not been explored. In this paper we investigate a freestanding $MnPS_3$ single layer using momentum-resolved electron-energy-loss spectroscopy (MREELS). EELS has been extensively used to study the nature of electronic excitations in freestanding layers [24–29]. There are several reasons for this including (1) high spatial resolution; (2) ability to study freestanding single layers. Most other spectroscopy methods on the other hand can only study single layers on a substrate; and (3) ability to investigate the momentum dependence of various excitations.

In EELS the measured single-scattering spectra are described by the energy-loss function (ELF), which is related to the dielectric function as ELF $\propto \mathrm{Im}[-1/\varepsilon(q,\omega)]$, where $\varepsilon(\boldsymbol{q},\omega)$ is the complex dielectric function [30–35].

The scattering geometry of an EELS experiment is presented in Fig. 2. In the EELS experiment, incident electrons characterized by energy E_0 and momentum k_0 are inelastically scattered at a scattering angle θ, where the momentum transfer between the probe electron and the electrons in the solid is given by $\hbar\boldsymbol{q}$. The scattering vector $\boldsymbol{q}$ is given by $\boldsymbol{k_0}–\boldsymbol{k}'$, where $\boldsymbol{k_0}$ and $\boldsymbol{k}'$ are the wave vectors of incident and inelastically scattered electrons, respectively [31,32]. For low scattering angles the momentum transferred by the inelastically scattered electron is related to the scattering angle through $\boldsymbol{q}^2 = \boldsymbol{k}_0^2(\theta^2 + \theta_E^2)$, where θ and θ_E are the scattering and characteristic angles, respectively. For an incident electron energy E_0 and energy loss ΔE the characteristic angle is

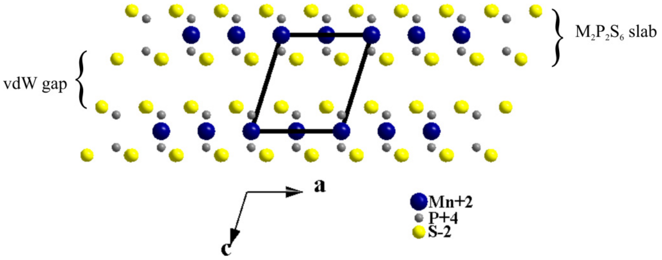

FIG. 1. Crystallographic bulk structure of $MnPS_3$ viewed along the *b* axis ([010] direction). A single $MnPS_3$ layer ($Mn_2P_2S_6$ slab) and the vdW gap between individual $MnPS_3$ layers are also indicated.

given by $\theta_E = \Delta E/2E_0$. The scattering wave vector $\boldsymbol{q}$ can be decomposed into momentum transfer parallel to the beam ($\boldsymbol{q}||$) and perpendicular to the beam direction ($\boldsymbol{q}\perp$). For small scattering angles, θ, $\boldsymbol{q}\perp = \boldsymbol{k}_0 \sin\theta \approx \boldsymbol{k}_0\theta$ and $\boldsymbol{q}|| = \boldsymbol{k}_0\,(\Delta E/2E_0)$. For the low-energy losses investigated in this paper ($\Delta E < 30$ eV), $\boldsymbol{q}||$ is very small and momentum transfer is mostly perpendicular to the electron beam ($\boldsymbol{q}\perp \approx \boldsymbol{k}_0\theta$) [26].

II. EXPERIMENTAL DETAILS

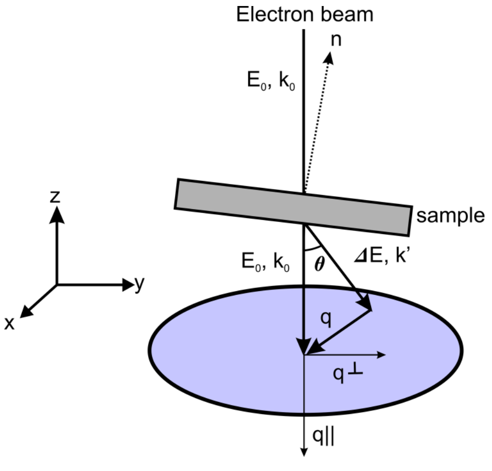

FIG. 2. Scattering geometry of an EELS experiment where the incident electron beam is characterized by energy E_0 and momentum k_0. The inelastically scattered electrons are characterized by an energy loss ΔE and momentum k'. The momentum transfer q can be decomposed into the component parallel to the electron beam, $q||$ and perpendicular to the electron beam $\boldsymbol{q}\perp$.

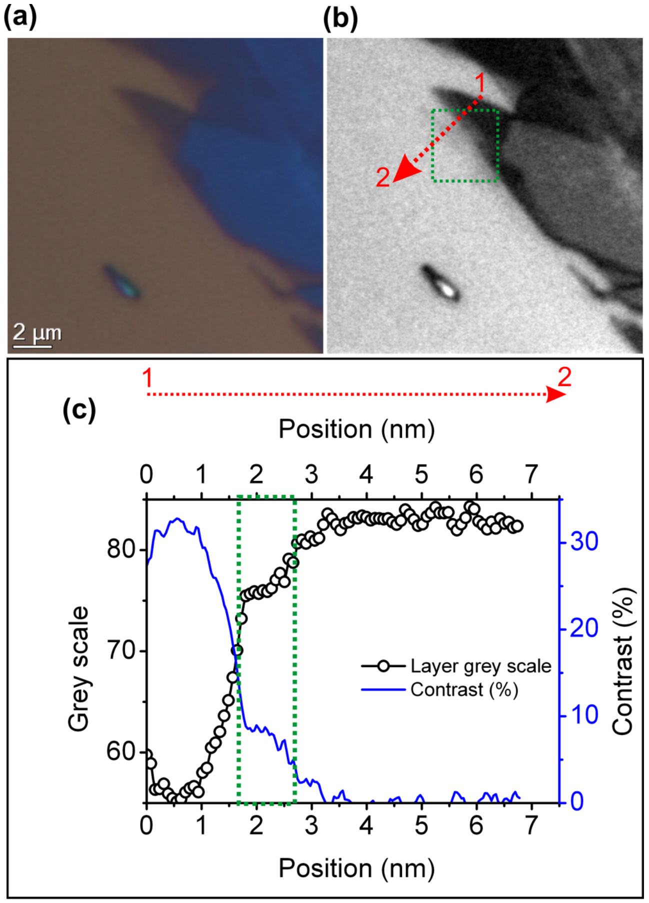

FIG. 3. $MnPS_3$ layers on SiO_2/Si substrate. (a) Under an optical microscope. (b) Green-channel image. (c) Comparison between grayscale values across $MnPS_3$ layers and SiO_2/Si substrate (open sphere) and calculated contrast (solid line) profiles along the $MnPS_3$ flakes and SiO_2/Si substrate obtained from positions 1 to 2.

The $MnPS_3$ layers investigated in this work were prepared from bulk $MnPS_3$ material using the mechanical exfoliation method. The thickness of the $MnPS_3$ layers obtained during the exfoliation process was estimated using the optical contrast of $MnPS_3$ layers on a SiO_2/Si substrate. This approach has already been successfully used to determine the number of layers in many two-dimensional layered materials including graphene, transition-metal dichalcogenides, as well transition-metal thiophosphates [36–39]. The method relies on the changes in the optical contrast of a SiO_2/Si substrate as a function of the nature and number of layers on it. The contrast is determined from the difference in grayscale values between a layer or a number of layers lying on the substrate and the substrate. This is done using a green channel image of the layers and the substrate to mimic contrast through illumination with green light. In this case contrast C is determined as $C = I_{\rm lay} - I_{\rm sub}/I_{\rm sub} + I_{\rm layer}$, where $I_{\rm sub}$ is the grayscale value at the SiO_2/Si substrate and $I_{\rm lay}$ is the grayscale value on the $MnPS_3$ layers. The obtained experimental contrast is then compared to expected layer contrast obtained through calculations for varying layers thicknesses and substrate thickness. The expected contrast for a single $MnPS_3$ layer on a SiO_2/Si substrate was calculated using the Fresnel-law-based model described in literature [36,38]. The parameters used during the calculation of contrast for $MnPS_3$ layers are thickness of the SiO_2, expected thickness of a single $MnPS_3$ layer, and the complex dielectric functions of $MnPS_3$, SiO_2, and Si. Using a SiO_2 layer thickness of 90 nm, $MnPS_3$ single-layer thickness of 0.67 nm, and refractive index of 2.41 for $MnPS_3$ [13], we calculated an expected contrast value of 7% for a single $MnPS_3$ layer. Figure 3(a) shows an image of exfoliated $MnPS_3$ layers on a SiO_2/Si as observed in the optical microscope.

Figure 3(b) shows the green-channel image of the $MnPS_3$ layers on SiO_2/Si substrate obtained from Fig. 3(a) using the software IMAGE J. The calculated contrast (solid curve) and grayscale values (open spheres) are shown in Fig. 3(c) as a function of position across the $MnPS_3$ layers and the SiO_2/Si substrate. The regions marked by dotted rectangle in Figs. 3(b) and 3(c) correspond to a contrast of 7%. This corresponds to the expected calculated contrast for a single $MnPS_3$ layer on SiO_2/Si substrate. The exfoliated $MnPS_3$ layers were then transferred onto perforated carbon sample grids for transmission electron microscopy (TEM) investigations. TEM investigations were done on freestanding layers lying on top of a hole in the supporting TEM sample grids. EELS spectra were acquired using a Gatan-Tridiem spectrometer attached to a Titan 80–300-kV TEM operating at 80 kV. The energy and momentum resolutions were determined to be 0.60 eV and 0.05 $Å^{-1}$, respectively. Short exposure times on the order of 0.05–0.1 s were used during the acquisition of the spectrum.

We also calculated band structure and theoretical spectra from bulk and single $MnPS_3$ layer in order to interpret and understand the nature and origins of spectral features observed in the experiments. The electronic structure and theoretical spectra were obtained within the density-functional-theory (DFT) framework, using the full potential linearized augmented plane-wave approximation as implemented in WIEN2K code. The exchange and correlation energy were described within the generalized gradient approximation (GGA) with the Perdew-Burke-Ernzerhof exchange-correlation functional. The calculations presented here were based on a monoclinic unit-cell space group $C2/m$ for bulk $MnPS_3$ and a trigonal unit-cell space group P-$31m$ for single-layer $MnPS_3$. The lattice parameters used during the calculations were $a = b = 6.077$ Å for the single-layer $MnPS_3$ and $a = 6.077$ Å, $b = 10.552\ 40$ Å, $c = 6.7960$ Å for bulk $MnPS_3$ [2,40]. A 20-Å vacuum slab was used to reproduce a DFT calculation on a single $MnPS_3$ layer. We used muffin-tin radii of 1.96, 2.5, and 1.86 a.u. for S, Mn, and P atoms, respectively. The parameter $R_{\mathrm{mt}*}K_{\max}$ was set to 7, where R_{mt} is the smallest atomic sphere radius in the unit cell and $K_{\max}$ is the magnitude of the largest K vector. The numbers of k points in the irreducible part of the Brillouin zone were 69 and 52 for bulk $MnPS_3$ and single-layer $MnPS_3$, respectively. The GGA + U method, which refers to the generalized gradient approximation (GGA) with the Hubbard parameter U (GGA + U), was used in order to treat the effects of local Coulomb interactions due to Mn-3d electrons. The value of the effective Coulomb parameter was set to $U_{\mathrm{eff}} = 5$ eV for both sets of calculations. In addition, AFM supercells were used for both bulk and single-layer $MnPS_3$. The GGA + U method underestimates the band-gap value in insulators and therefore a scissor operator of 2 eV was used during the optical calculations. We did not include local field effects (LFE) in our calculations. Random-phase approximation calculations without LFE have been shown to reproduce the EELS spectra for low momentum values quite well [35–37].

III. RESULTS AND DISCUSSION

A. Position and nature of the observed peaks

Figure 4 presents the experimental EELS spectra from bulk (dotted curve) and single $MnPS_3$ layer (solid curve), respectively. The spectra are not momentum resolved and are considered to be integrated over all q.

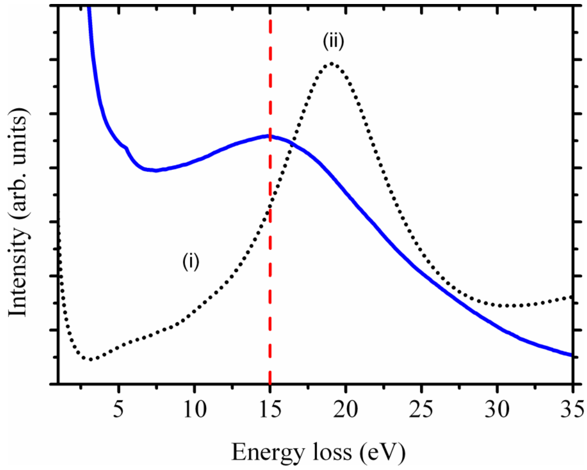

FIG. 4. Experimental electron-energy-loss spectra from bulk $MnPS_3$ layer (dotted curve) and a single $MnPS_3$ layer (solid curve) obtained perpendicular to the $MnPS_3$ layers. The dotted line at position 15 eV is a guide for the eye.

Both bulk and single-layer $MnPS_3$ are anisotropic and hence the ELF varies with the crystallographic direction. The experiments presented here were conducted with the electron beam parallel to the c axis [001]. For low-energy losses investigated here the direction of momentum transfer is mostly perpendicular to the direction of the electron beam. Therefore the experiments probed the spectra parallel to the $MnPS_3$ plane. The spectra displayed in Fig. 4 are divided into energy regions (i) between 0 and 15 eV and (ii) above 15 eV. The energy region (i) is characterized by small peaks between 0 and 10 eV in both single-layer and bulk $MnPS_3$. In bulk $MnPS_3$ the spectra in region (ii) is dominated by a peak at around 19 eV. On the other hand the most prominent peak in single-layer $MnPS_3$ is observed at 15 eV. We note that the main spectral difference between the single-layer and bulk $MnPS_3$ is observed in energy region (ii). In order to describe the observed spectra differences between single-layer and bulk $MnPS_3$ it is important to identify the nature and origin of the excitations giving rise to the observed spectral features.

The region of EELS spectra shown in Fig. 4 is known as the valence EELS (VEELS) and is characterized by energy losses found below 50 eV. The excitations observed in the VEELS region include relativistic excitations, surface excitations, excitons, interband transitions, and plasmon excitations [31–35]. The VEELS spectrum in bulk $MnPS_3$ has been shown to be mostly dominated by plasmon excitations and interband transitions [22]. In order to differentiate these two types of excitations it is necessary to derive and study the behavior of the dielectric function [33,34]. This can be done through the derivation of experimental dielectric function from single-scattering experimental EELS spectra or through theoretically derived spectra and dielectric functions [34,41,42]. In this paper we use the theoretical approach. The motivation for this is that the theoretical approach also provides the possibility to investigate if the observed experimental difference in the spectra between bulk and single layers can be theoretically reproduced by calculations. From the electronic structure and spectra calculations we obtained band gaps for bulk and

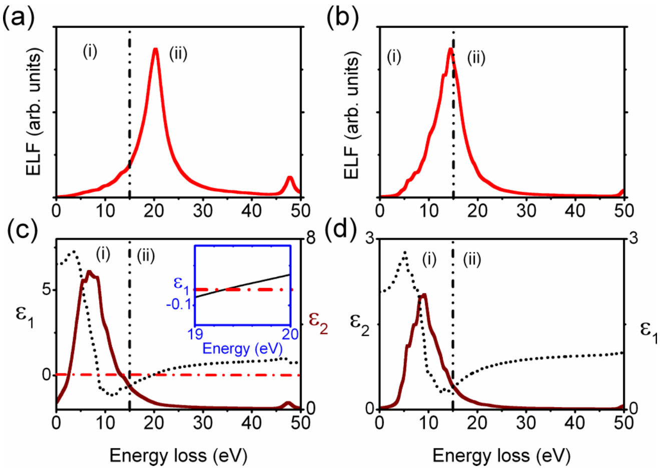

FIG. 5. Calculated ELF parallel to the *x* axis [100] for (a) bulk $MnPS_3$ and (b) single $MnPS_3$ layer. Calculated imaginary part of the dielectric function ε_2 (solid curve) and real part of the dielectric function ε_1 (dotted curve) for (c) bulk and (d) single-layer $MnPS_3$. The inset in (c) shows the position at which the ε_1 curve cuts the energy axis with a positive slope.

single-layer $MnPS_3$ on the order of 1 eV. The band gaps for bulk $MnPS_3$ and single layer have been determined to be 3.0 and 3.14 eV, respectively [8,15]. This is an underestimation of the band gap of approximately 2 eV with regard to experimental values. For this reason a scissor operator of approximately 2 eV was used during the calculation of optical properties for both bulk and single-layer $MnPS_3$ [41].

Figures 5(a) and 5(b) display the calculated ELFs at $q \sim 0\,\text{Å}^{-1}$ and parallel to the *x* direction for bulk and single-layer $MnPS_3$, respectively. Similar to the experimental spectra, the calculated ELFs in Fig. 5 are also divided into energy regions (i) and (ii). Comparing both spectra we observe that the energy region (i) is similar in both calculated ELFs for single-layer and bulk $MnPS_3$. The most significant difference between calculated ELFs for single and bulk $MnPS_3$ is observed in energy region (ii). The calculated ELF from bulk $MnPS_3$ is characterized by a large peak at ∼19 eV. In the calculated ELF for single $MnPS_3$ layer the peak maximum is at 15 eV. This is similar to the behavior observed in the experimental EELS spectra. The calculated ELFs presented in Figs. 5(a) and 5(b) can be also expressed as $\text{ELF} = \text{Im}[-1/\varepsilon(q,\omega)] = \varepsilon_2/(\varepsilon_1^2 + \varepsilon_2^2)$, where ε, ε_1, and ε_2 are the dielectric function, real, and imaginary parts of the dielectric function, respectively [31–34]. Figures 5(c) and 5(d) display the ε_1 (dotted line) and ε_2 (solid line) curves calculated for bulk and single-layer $MnPS_3$, respectively. The ε_2 curve is similar in both bulk and single-layer $MnPS_3$ and is characterized by peaks in the energy-loss region between 0 and 15 eV, after which the ε_2 curve decreases steadily at higher energies. In general the peaks observed in the imaginary part of the dielectric function ε_2 are mostly due to interband transitions [33–35]. In bulk $MnPS_3$ the interband transitions have been shown to be of the following nature: (1) crystal-field excitations involving *d*-*d* excitations; (2) charge-transfer excitations involving between S-*p* and P-*p* bands to Mn 3*d* states; and (3) transitions between S-*s*, P-*s* states with the hybridized antibonding S-*p*, P-*p* states [22]. These transitions are mainly found in the energy region between 0 and 15 eV in both single-layer and bulk $MnPS_3$. The ε_1 curve on the other hand shows an important difference between bulk and single-layer $MnPS_3$. As shown in Fig. 5(c), for bulk $MnPS_3$ as the ε_2 curve decreases toward zero, the ε_1 curve crosses the energy axis with a positive slope after 19 eV. The crossing of the ε_1 curve is shown in the inset of Fig. 5(c). At this energy the condition for plasmon excitation is thus fulfilled since $\varepsilon_1 \to 0$ and ε_2 is small [33–35]. The large peak in region (ii) in bulk $MnPS_3$ is therefore confirmed to be a volume plasmon peak. However in contrast to the bulk structure in $MnPS_3$ single layer the ε_1 curve does not vanish and is characterized by positive values for all energy losses.

This is a behavior commonly observed in damped plasmons. A damped plasmon does not fulfill the plasmon conditions $\varepsilon_1 \to 0$ and ε_2 is small. In addition to having positive values of ε_1, damped plasmons also lead to the broadening of the spectra. Indeed, our calculations show that the calculated spectra for single layer are broadened with respect to that of bulk $MnPS_3$. The damping of the plasmon peak is due to the influence of interband transitions which are observed in the vicinity of the plasmon excitations. In this case these are interband transitions observed in the energy range up to 15 eV. Damped plasmons have also been observed in graphite with increased interlayer distance [43]. In graphite, the redshift of the plasmon with increased interlayer distance brings it into the vicinity where interband transitions are strong such that collective excitations are mixed with single-particle excitations. This leads to the damping of the plasmon excitation. Damped plasmons have been shown in several two-dimensional layers including transition-metal dichalogenide single layers, and *h*-BN [43–46]. In addition, damped plasmons have also been observed in transition-metal oxides [47–49]. In $YBa_2Cu_3O_{7-\delta}$ the real part of the dielectric function (ε_1) in superconducting oxides is positive in the region where one expects the plasmon excitation [47]. This has been shown to be due to plasmon excitations being damped by interband transitions in the vicinity.

We also compared the observed plasmon peaks positions for bulk and $MnPS_3$ single layer in the experimental and calculated spectra with the peak positions calculated using Horie's formula $(\hbar\omega_g)^2 = (\hbar\omega_f)^2 + (E_g)^2$, where $\hbar\omega_g$ is the plasmon energy of an insulator, $\hbar\omega_f$ is the free-electron plasmon energy, and E_g is the band gap [50–53]. Free-plasmon energy is given as $\hbar\omega_f{}^2 = [\hbar(Ne^2/(\varepsilon_0 m_e)]$, where N is the density of outer-shell valence electrons, m_e is the effective mass, and ε_0 is the permittivity of free space [30]. Horie's formula has been shown to be quite accurate in determining the position of plasmon peaks in semiconductors and insulators [51]. In general, the plasmon energy position shows a general dependence (dispersion) with momentum transfer q which can be expressed as $\hbar\omega(q) = \hbar\omega_f + \alpha(\hbar/m)q^2$, where α is the polarizability [52,53]. The spectrum for single-layer $MnPS_3$ presented in Fig. 5(b) was calculated based on a single layer approximated using a single $M_2P_2S_6$ slab [17,20]. This slab contains a total of 60 valence electrons including 10*e* from $2 \times \text{Mn}^{+\text{II}}(3d^5, 4s0)$; 2*e* from $2 \times \text{P}^{+\text{IV}}(3s^1, 3p0)$; 48*e* from $6 \times \text{S}^{-\text{II}}(3s^2, 3p6)$ [20]. The position of the plasmon peaks in single ($Mn_2P_2S_6$ slab calculated using Horie's formula is 14.6 eV. This is close to the experimentally obtained value.

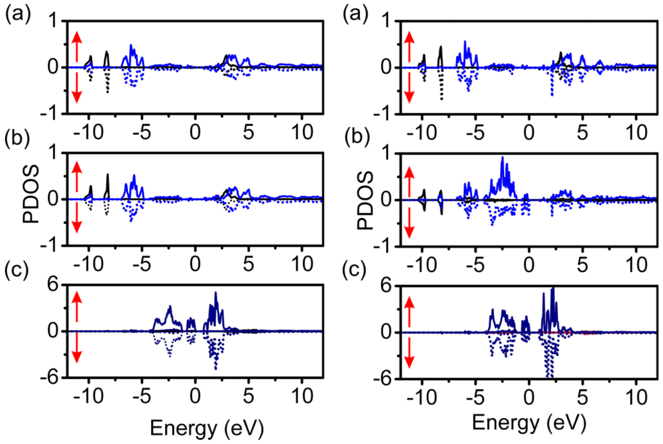

FIG. 6. Spin-up (↑) and spin-down (↓) PDOS for (a) bulk P-*s* and P-*p*, (b) bulk S-*s* and S-*p*, (c) bulk Mn-*s* and Mn-*d*, (d) single-layer P-*s* and P-*p*, (e) single-layer S-*s* and S-*p*, and (f) single-layer Mn-*s* and Mn-*d*.

The bulk $\mathrm{MnPS_3}$ structure is on the other hand represented as $\mathrm{Mn_4P_4S_{12}}$. The calculated theoretical value for plasmon energy in bulk $\mathrm{MnPS_3}$ is 20.4 eV, which is close to the obtained experimental value [22]. The calculated values for free plasmons are 14.3 and 20.2 eV for single-layer and bulk $\mathrm{MnPS_3}$, respectively. Since the volume plasmon is a collective excitation of all valence electrons, the total valence electron density in both structures will determine the plasmon energy position in both bulk and single-layer $\mathrm{MnPS_3}$. This is directly related to the electronic structure of both single-layer and bulk $\mathrm{MnPS_3}$. We therefore compared the electronic structure of single and bulk $\mathrm{MnPS_3}$ layers in the valence region.

The spin-up (↑) and spin-down (↓) partial density of states (PDOS) in bulk and single-layer $\mathrm{MnPS_3}$ are displayed in Fig. 6. Figures 6(a)–6(c) display the bulk $\mathrm{MnPS_3}$ for P-*s*/P-*p*, S-*s*/S-*p*, and Mn-*s*/Mn-*d* respectively. The corresponding PDOS for the $\mathrm{MnPS_3}$ single layer are displayed in (d) and (e) for P-*s*/P-*p* and S-*s*/S-*p*, respectively. Mn-3*d* states dominate the energy states found between −5 eV and the top of the valence band. P-*p* and S-*p* states are found below −5 eV. From the PDOS results presented in Fig. 6 we observe that the electronic structures in both single-layer and bulk $\mathrm{MnPS_3}$ are very similar. In both structures the valence region between −10 eV and the Fermi level contains contributions from Mn-4*s*, Mn-3*d*, P-3*s*, P-3*p*, S-3*s*, and S-3*p* states. Therefore, the electronic states used to calculate the plasmon peak positions in the Horie approach are similar in both bulk and single-layer $\mathrm{MnPS_3}$. We used density of states calculations to confirm that the valence electronic structures in both structures are similar and the only difference between the two is the number of valence electrons per unit cell.

B. Momentum dependence of the observed peaks

We used momentum-resolved EELS spectra to determine the dispersion behavior of the observed plasmon excitations in both single-layer and bulk $\mathrm{MnPS_3}$. The momentum information was accessed by acquiring EELS spectra in the reciprocal space (at the diffraction plane of the TEM) [27,31,32]. By using a selecting slit placed above the spectrometer, the electrons which have been scattered at a certain given scattering angle can be selected and allowed into the spectrometer. The direction and magnitude of momentum transfer $|\boldsymbol{q}|$ are then obtained from the projected direction and magnitude of the scattering angles in the electron diffraction pattern [32]. Figure 7(a) shows an electron diffraction pattern from bulk $\mathrm{MnPS_3}$ layer obtained with the sample oriented parallel to the [001] orientation. The diffraction pattern was indexed based on monoclinic $\mathrm{MnPS_3}$ structure with space group $C2/m$. The dotted rectangle shows the pair of 2 0 0 and −2 0 0 diffraction spots that were selected using a slit to acquire momentum-resolved EELS spectra. This corresponds to MREELS spectra parallel to the Γ-A direction of the bulk $\mathrm{MnPS_3}$ Brillouin zone (BZ). The respective diffraction pattern for $\mathrm{MnPS_3}$ single layer is shown in Fig. 7(b). The structure for $\mathrm{MnPS_3}$ single layer was approximated with a trigonal space group P-31m. The direction probed in the single layer is therefore parallel to −1 2 0 and 1 −2 0 spots.

The resulting momentum-resolved EELS spectrum shows energy loss ΔE (horizontal axis) as a function of momentum q (vertical axis). The obtained MREELS spectrum along the Γ-A direction in bulk $\mathrm{MnPS_3}$ BZ is shown in Fig. 7(c). Momentum-resolved spectra at individual momentum-transfer values q are then obtained from intensity profiles at various q of the MREELS spectra shown in Fig. 7(c).

These are presented in Figs. 8(a) and 8(b) for bulk and single $\mathrm{MnPS_3}$ layers, respectively. The spectra are shown for a range of momentum-transfer values between 0 and 1 $\mathrm{\mathring{A}^{-1}}$. We observe that the plasmon peak for the single-layer $\mathrm{MnPS_3}$ disperses from a value of ∼15 to 23 eV. The volume plasmon peak in bulk $\mathrm{MnPS_3}$ disperses from a value of 18 to 24 eV. In addition, the width of the peaks increases with increased momentum transfer as a result of increased Landau damping of the plasmon excitation.

The dispersion curves for both bulk and single-layer $\mathrm{MnPS_3}$ are shown in Figs. 9(a) and 9(b), respectively. We also fitted the dispersion curves with quadratic ($Y = A_0 + Bq^2$) and square root ($Y = A_0 + Bq^{0.5}$) functions for bulk and single-layer $\mathrm{MnPS_3}$, respectively. It can be seen that the dispersion curve for bulk $\mathrm{MnPS_3}$ can be described using the quadratic dispersion behavior characteristic for a bulk plasmon [32,43,54–56]. On the other hand, the dispersion curve for the single-layer $\mathrm{MnPS_3}$ can be described by a square-root dispersion which is characteristic for a two-dimensional plasmon [57–59].

It is important to note that the determination of the dispersion curves displayed in Fig. 9 is influenced by several factors. The first influencing factor is the increased effects of surface and relativistic losses for very thin samples [30,60,61]. However, the intensity (I) of surface losses decreases rapidly with increasing momentum transfer in the order of $I \sim q^{-3}$. This is in contrast to bulk losses whose intensity decreases as $I \sim q^{-2}$ [30,57]. Therefore, the influence of these effects on the obtained MREELS spectra is minimized by avoiding spectra at very low momentum values of $|q| \approx 0\ \mathrm{\mathring{A}^{-1}}$ [30,60]. The analysis of the nature of surface plasmons in $\mathrm{MnPS_3}$ is shown in more detail in the Appendix. The second factor arises from uncertainties from low signal-to-noise at high momentum-transfer values and finite momentum and energy

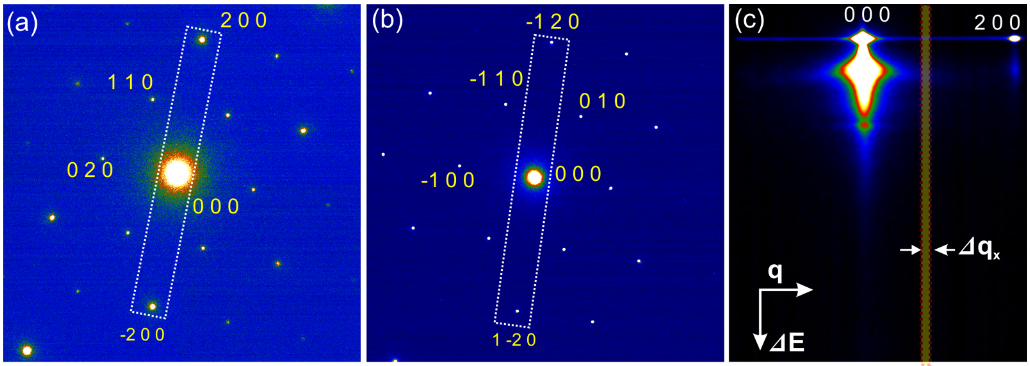

FIG. 7. Indexed selected area electron diffraction from (a) bulk $MnPS_3$ obtained along the [001] crystalline direction. The diffraction pattern is indexed using the monoclinic bulk structure with space group $C\,2/m$. (b) Single-layer $MnPS_3$ indexed according to the trigonal structure with space group P-$31m$ (c) Momentum-resolved electron-energy-loss spectra (q vs ΔE) parallel to the 2 0 0 and −2 0 0 diffraction spot direction. The dotted rectangle shows the integration window width $\Delta q_x = 0.05\ \text{Å}^{-1}$ used to obtain individual spectra at specific q.

resolutions. The error bars in Fig. 9 represent the uncertainty in determining the energy and momentum positions from the obtained momentum-resolved EELS spectra. The uncertainty in determining the peak position in the energy axis can be determined as $\sigma = \sqrt{\Delta E^2 + \delta E^2}\,/\sqrt{N}$, where ΔE, δE, and N are peak width, instrumental energy dispersion, and peak counts, respectively [54]. The accuracy in determining the momentum value is limited by the integration window Δq_x used to obtain the q intensity profiles [25]. This was determined to be $0.05\ \text{Å}^{-1}$ The last factor is the influence from elastic-inelastic multiple-scattering effects which increase at increasing momentum transfer [62,63]. Correction for multiple-scattering effects in momentum-resolved EELS especially at large q remains a challenging task. However, an approach to remove multiple scattering has already been developed which involves deconvolution of a q integrated spectrum obtained from momentum-resolved spectra obtained at large momentum values [63]. Another approach is to work with the MREELS spectra at low momentum-transfer values since the elastic-inelastic scattering effects increase at large momentum-transfer values. Indeed, it has been shown that the elastic-inelastic multiple-scattering effects are small for small momentum-transfer values ($|\boldsymbol{q}| < 1\ \text{Å}^{-1}$) [62]. This is the approach that was used in this paper. Within the momentum range where we expect reduced effects from surface, relativistic, and

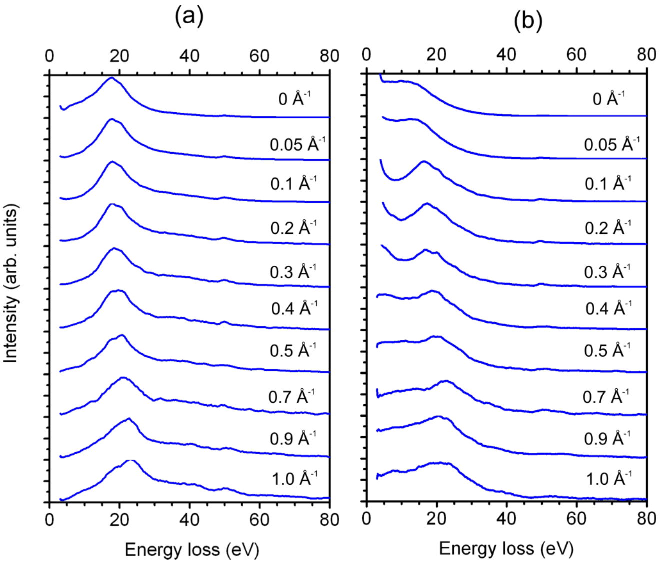

FIG. 8. Momentum-resolved EELS spectra in (a) bulk $MnPS_3$ and (b) single $MnPS_3$ layer for various momentum-transfer values.

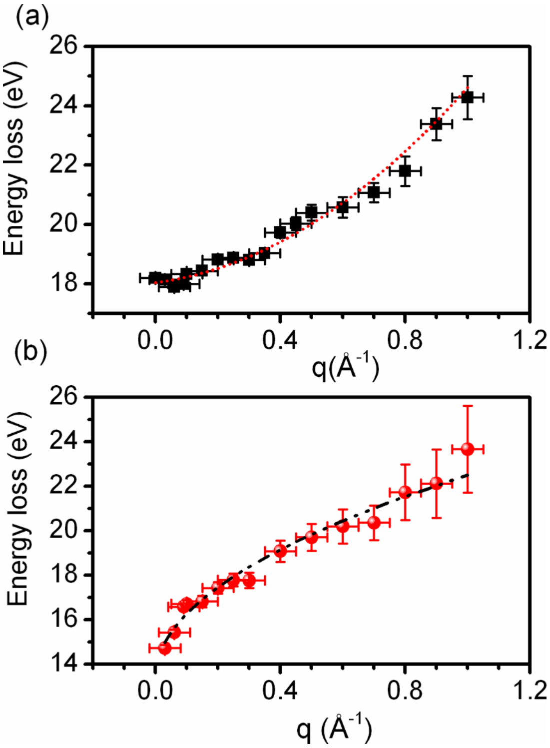

FIG. 9. The dispersion of the plasmon peaks for (a) bulk $MnPS_3$ and (b) single-layer $MnPS_3$. The error bars represent the uncertainty due to the integration window of the momentum $\Delta q_x = 0.05\ \text{Å}^{-1}$ and in measuring the plasmon peak energy position. The dotted curve and dashed-dotted-dotted curves in (a) and (b) represent fitting of the dispersion curves with quadratic and square-root functions, respectively.

elastic-inelastic scattering, $0.1 \leqslant q \leqslant 1$ Å^{-1}, we observe that the dispersion curves indeed follow a quadratic dispersion for bulk and square-root dispersion for single layer. The results presented here show that the position of the plasmon peak and its dispersion are sensitive to the dimensionality of the MnPS$_3$ layer. This also demonstrates that EELS spectra can also be used to differentiate between bulk and single-layer MnPS$_3$.

IV. CONCLUSIONS

In this paper we have explored the spectroscopic properties of freestanding MnPS$_3$ layers using momentum-resolved electron-energy-loss spectroscopy and compared them to bulk MnPS$_3$. The MnPS$_3$ single layers investigated in this work were obtained through exfoliation from bulk MnPS$_3$ flakes. We show that the EELS spectra of single MnPS$_3$ layers are distinct from bulk structure, which provides a method to differentiate single-layer MnPS$_3$ from bulk structures. The volume plasmon peak is shifted from 19 eV in bulk MnPS$_3$ to 15 eV in single layer. Theoretical calculations show that this peak corresponds to a damped plasmon peak in single-layer MnPS$_3$. We also investigated the dispersion characteristics of plasmon excitations in bulk and single MnPS$_3$ layer. The plasmon dispersion curve for the single-layer MnPS$_3$ follows the square-root dispersion which is characteristic for a 2D plasmon. This shows the effects of dimensionality on the observed electronic excitations in MnPS$_3$.

ACKNOWLEDGMENTS

The authors acknowledge funding from the German Research Foundation (DFG) and the Ministry of Science, Research and the Arts (MWK) of the federal state Baden-Württemberg, Germany in the frame of the SALVE (Sub-Angstroem Low-Voltage) project.

APPENDIX: SURFACE PLASMONS IN MnPS$_3$

In our paper, using experimental electron-energy-loss spectroscopy supported by (1) DFT calculations and (2) Horie calculations, we showed that a single MnPS$_3$ layer is characterized by redshifted plasmon peak positioned at ~ 15 eV. However, it is well known that the probability of exciting surface plasmons increases with decreasing sample thickness [30,60]. We therefore expect to see both surface plasmons and bulk plasmons in MnPS$_3$ single layer. Using the free-electron model, the surface plasmon in MnPS$_3$ single layer is expected to be found at the energy position given by $\hbar\omega_s = (\hbar\omega_f)/\sqrt{2}$, where $\hbar\omega_f$ is the value of the bulk plasmon. This corresponds to the energy region between 10 and 14 eV in bulk MnPS$_3$. This is in the same region where we expect to see a characteristic volume plasmon for the single MnPS$_3$ layer. However, it is also known that surface and volume plasmons have different momentum dependency [60]. This fact is normally used to differentiate surface and volume plasmons. Surface plasmons can be well distinguished from bulk plasmons in that they decay rapidly with increasing momentum transfer. In the following analysis we show using experiments and surface calculations that the peak we observed in single-layer MnPS$_3$ is a characteristic of the layer and is not due to surface plasmons.

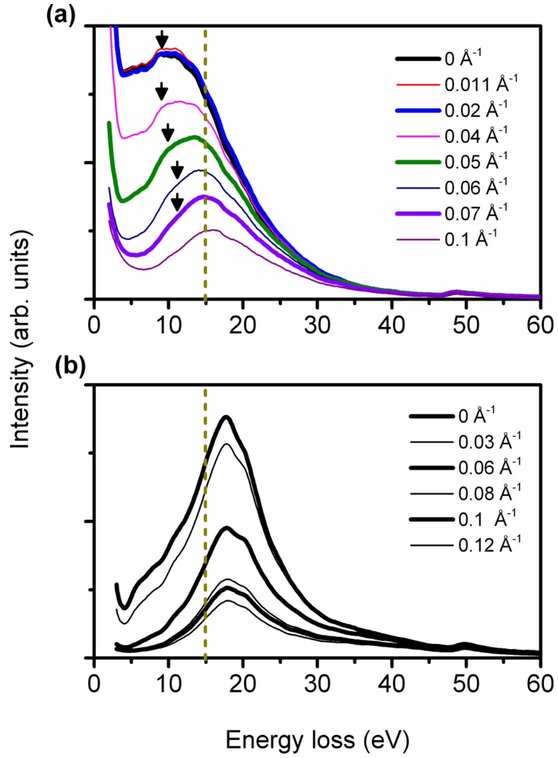

FIG. 10. Experimental EELS spectra for (a) MnPS$_3$ single layer and (b) MnPS$_3$ bulk showing spectra at various momentum-transfer values between 0 and 0.1 Å^{-1}. The effects of surface plasmons can be clearly seen between 10 and 13 eV (arrows) in the single layer. The dotted line at 15 eV is a guide for the eye.

1. Experimental results on surface plasmons in MnPS$_3$

In Fig. 10(a) we show experimental spectra for a MnPS$_3$ single layer for momentum-transfer values between 0 and 0.1 Å^{-1}. The arrows show the position of the surface plasmons which can be clearly seen between 10 and 13 eV. The dotted line at 15 eV is a guide for the eye. From the figure it is clear that the intensity of the surface plasmons decays rapidly with increasing momentum transfer such that above 0.07 Å^{-1} they become negligible. It is important to emphasize that in single-layer MnPS$_3$ both surface and bulk plasmons occur. The intensity of volume plasmons is hidden by the very intense surface plasmons at low momentum values. Above 0.07 Å^{-1} the volume plasmon can be clearly distinguished. In Fig. 10(b) we show experimental spectra for bulk MnPS$_3$ single layer for momentum-transfer values between 0 and 0.1 Å^{-1}. In contrast to single MnPS$_3$ layer the intensity at low momentum transfers is dominated by the bulk plasmons and no significant surface plasmons can be seen.

2. Comparison with surface plasmon calculations

Here we show the results of calculations showing the probability of exciting surface losses for MnPS$_3$ layers of various thicknesses. The surface calculations shown here are based on the local Kröger formalism where the loss probability is quantitatively obtained as a function of scattering angle (θ) and energy loss (ΔE) [64].

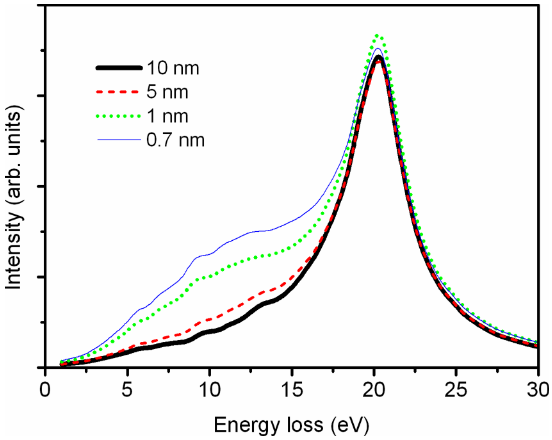

FIG. 11. Calculated probability for surface losses for $MnPS_3$ sample thickness of 10, 5, 1, and 0.7 nm.

The Kröger formalism accounts for the relativistic effects in the spectra including Cherenkov losses as well as surface plasmons. The band-structure-based DFT approach used in the paper does not take these effects into consideration. In the calculations presented here we used the approach developed by Bolton and Chen to calculate surface excitations for a vacuum/$MnPS_3$/vacuum layered model [64–66]. The input for these calculations is the $MnPS_3$ dielectric constant which was obtained from the DFT calculations.

Figure 11 shows the calculated probability to excite surface plasmons for $MnPS_3$ sample thicknesses of 10, 5, 1, and 0.7 nm. The spectra are not momentum resolved and are considered to be integrated over all scattering angles. As observed in the experiment (Fig. 10), surface plasmons begin to dominate in the energy region 10–14 eV for small sample thicknesses. We used the dielectric constants for bulk $MnPS_3$ in order to determine where the surface plasmons are observed in bulk structures. Therefore, the bulk plasmon at 20 eV is still visible even for sample of 0.7 nm.

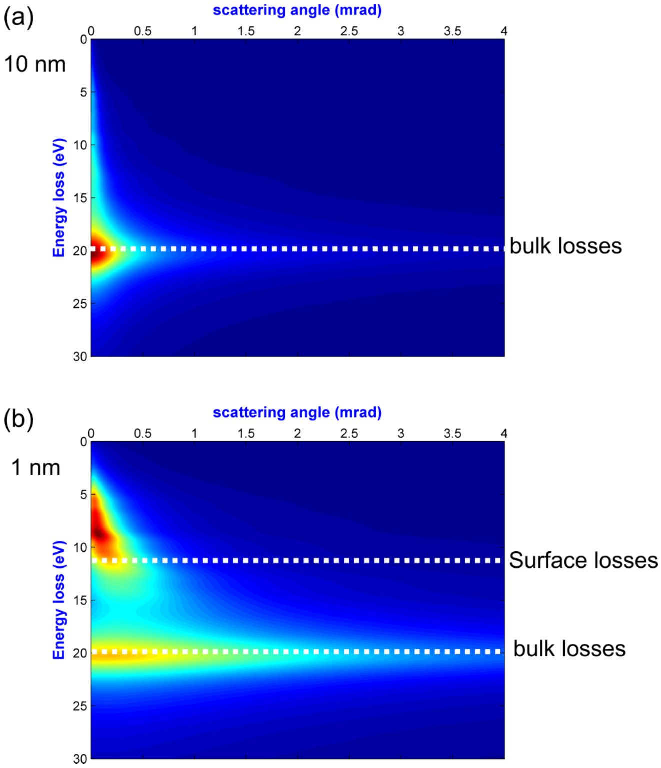

FIG. 12. Calculated scattering probabilities [energy loss (E), scattering angle (θ)] at 80 kV for $MnPS_3$ sample thickness of (a) 10 and (b) 1 nm. The positions of surface and bulk losses are indicated.

In addition, we also calculated the scattering probability of surface plasmons as a function of energy loss (ΔE) and scattering angle (θ). In Fig. 12(a) we show the calculated scattering probability spectra for a 10-nm-thick $MnPS_3$ film. In bulk structure the spectra are dominated by volume plasmons around 19–20 eV. In Fig. 12(b) we show the calculated scattering probability for a 1-nm-thick $MnPS_3$ slab. In contrast to bulk, the spectra are also characterized by increased losses due to surface plasmons around 10–14 eV. However, it can be clearly seen that the intensity of these surface plasmons decays rapidly with increasing scattering angle. They are observed to dominate the region in the scattering angles below 0.5 mrad. In our paper we investigated the dispersion parallel to the 200 direction in $MnPS_3$ with $|q| = 2.16\ \text{Å}^{-1}$. This corresponds to a scattering angle (θ) of 7.2 mrad. The calculated surface plasmons are shown to dominate the region in the scattering angles below 0.5 mrad which corresponds to momentum transfer of $0.15\ \text{Å}^{-1}$. This agrees very well with the experimental results shown in Fig. 10.

[1] R. Brec, Solid State Ionics **22**, 3 (1986).
[2] G. Ouvrard, R. Brec, and J. Rouxel, Mater. Res. Bull. **20**, 1181 (1985).
[3] P. A. Joy and S. Vasudevan, Phys. Rev. B **46**, 5425 (1992).
[4] A. R. Wildes, H. M. Ronnow, B. Roessli, M. J. Harris, and K. W. Godfrey, Phys. Rev. B **74**, 094422 (2006).
[5] M. Piacentini, F. S. Khumalo, G. Leveque, C. G. Olson, and D. W. Lynch, Chem. Phys. **72**, 61 (1982).
[6] V. Grasso and L. Silipigni, Rivista del Nuovo Cimento **25**, 1 (2002).
[7] R. Clement, J. Chem. Soc., Chem. Commun. **0**(14), 647 (1980).
[8] R. Brec, D. M. Schleich, G. Ouvrard, A. Louisy, and J. Rouxel, Inorg. Chem. **18**, 1814 (1979).
[9] M. A. Susner, M. Chyasnavichyus, M. A. McGuire, P. Ganesh, and P. Maksymovych, Adv. Mater. **29**, 1602852 (2017).
[10] J. Liu, X.-B. Li, D. Wang, W. M. Lau, P. Peng, and L.-M. Liu, J. Chem. Phys. **140**, 054707 (2014).
[11] K. Du, X. Wang, Y. Liu, P. Hu, M. I. B. Utama, C. K. Gan, Q. Xiong, and C. Kloc, ACS Nano **10**, 1738 (2016).
[12] B. L. Chittari, Y. Park, D. Lee, M. Han, A. H. MacDonald, E. Hwang, and J. Jung, Phys. Rev. B **94**, 184428 (2016).
[13] R. F. Frindt, D. Yang, and P. Westreich, J. Mater. Res. **20**, 1107 (2005).

[14] J.-U. Lee, S. Lee, J. H. Ryoo, S. Kang, T. Y. Kim, P. Kim, C.-H. Park, J.-G. Park, and H. Cheong, Nano Lett. **16**, 7433 (2016).

[15] X. Zhang, X. Zhao, D. Wu, Y. Jing, and Z. Zhou, Adv. Sci. (Weinh) **3**, 1600062 (2016).

[16] D. Mukherjee, P. M. Austeria, and S. Sampath, ACS Energy Lett. **1**. 367 (2016).

[17] V. Grasso, F. Neri, P. Perillo, L. Silipigni, and M. Piacentini, Phys. Rev. B **44**, 11060 (1991).

[18] P. A. Joy and S. Vasudevan, Phys. Rev. B **46**, 5134 (1992).

[19] V. Grasso, S. Santangelo, and M. Piacentini, Solid State Ionics **20**, 9 (1986).

[20] F. S. Khumalo and H. P. Hughes, Phys. Rev. B **23**, 5375 (1981).

[21] M. Piacentini, F. S. Khumalo, C. G. Olson, J. W. Anderegg, and D. W. Lynch, Chem. Phys. **65**, 289 (1982).

[22] Y. Ohno and S. Nakai, J. Phys. Soc. Jpn. **54**, 3591 (1985).

[23] H. Mercier, Y. Mathey, and E. Canadell, Inorg. Chem. **26**, 963 (1987).

[24] M. K. Kinyanjui, C. Kramberger, T. Pichler, J. C. Meyer, P. Wachsmuth, G. Benner, and U. Kaiser, Europhys. Lett. **97**, 57005 (2012).

[25] P. Wachsmuth, R. Hambach, M. K. Kinyanjui, M. Guzzo, G. Benner, and U. Kaiser, Phys. Rev. B **88**, 075433 (2013).

[26] C. T. Pan, R. R Nair, U. Bangert, Q. M. Ramasse, R. Jalil, R. Zan, C. R. Seabourne, and A. J. Scott, Phys. Rev. B **85**, 045440 (2012).

[27] S. C. Liou, C.-S. Shie, C. H. Chen, R. Breitwieser, W. W. Pai, G. Y. Guo, and M.-W. Chu, Phys. Rev. B **91**, 045418 (2015).

[28] H. C. Nerl, K. T. Winther, F. S. Hage, K. S. Thygesen, L. Houben, C. Backes, J. N. Coleman, Q. M. Ramasse, and V. Nicolosi, NPJ 2D Mater. Appl. **1**, 2 (2017).

[29] K. S. Thygesen, 2D Mater. **4**, 022004 (2017)

[30] R. F. Egerton, Rep. Progr. Phys. **72**, 016502 (2009).

[31] J. Fink, Adv. Electron. Electron Phys. **75**, 121 (1989).

[32] K. Zeppenfeld, Z. Phys. **243**, 229 (1971).

[33] H. Raether, *Excitation of Plasmons and Interband Transitions by Electrons* (Springer-Verlag, Berlin, 1980).

[34] R. D. Bringans and W. Y. Liang, J. Phys. C: Solid State Phys. **14**, 1065 (1981).

[35] H. R. Philipp and H. Ehrenreich, Phys. Rev. **129**, 1550 (1963).

[36] M. M. Benameur, B. Radisavljevic, J. S. Heron, S. Sahoo, H. Berger, and A. Kis, Nanotechnology **22**, 125706 (2011).

[37] H. Li, J. Wu, X. Huang, G. Lu, J. Yang, X. Lu, Q. Xiong, and H. Zhang, ACS Nano **7**, 10344 (2013).

[38] P. Blake, E. W. Hill, A. H. Castro Neto, K.S. Novosolev, D. Jiang, R. Yang, T. J. Booth, A. K. Geim, and E. W. Hill, Appl. Phys. Lett. **91**, 063124 (2007).

[39] G. Long, T. Zhang, X. Cai, J. Hu, C.-W. Choo, S. Xu, J. Shen, Z. Wu, T. Han, J. Lin, J. Wang, Y. Cai, R. Lortz, S. Mao, and N. Wang, ACS Nano **11**, 11330 (2017).

[40] A. Hashemi, H.-P. Komsa, M. Puska, and A. V. Krasheninnikov, J. Phys. Chem. C **121**, 27207 (2017).

[41] P. Moreau, V. Mauchamp, F. Pailloux, and F. Boucher, Appl. Phys. Lett. **94**, 123111 (2009).

[42] M. K. Kinyanjui, G. Benner, G. Pavia, F. Boucher, H.-U. Habermeier, B. Keimer, and U. Kaiser, Appl. Phys. Lett. **106**, 203102 (2015).

[43] A. G. Marinopoulos, L. Reining, A. Rubio, and V. Olevano, Phys. Rev. B **69**, 245419 (2004).

[44] F. J. Nelson, J.-C. Idrobo, J. D. Fite, Z. L. Miskovic, S. J. Pennycook, S. T. Pantelides, J. U. Lee, and A. C. Diebold, Nano Lett. **14**, 3827 (2014).

[45] K. Andersen and K. S. Thygesen, Phys. Rev. B **88**, 155128 (2013).

[46] R. J. Nicholls, J. M. Perkins, V. Nicolosi, D. W. McComb, P. D. Nellist, and J. R. Yates, J. Phys. Conf. Ser. **371**, 012060 (2012).

[47] S. Huotari, M. Cazzaniga, H.-C. Weissker, T. Pylkkänen, H. Müller, L. Reining, G. Onida, and G. Monaco, Phys. Rev. B **84**, 075108 (2011).

[48] H. Romberg, N. Nücker, J. Fink, T. Wolf, X.-X. Xi, B. Koch, H. P. Geserich, M. Durrler, W. Assmus, and B. Gegenheimer, Z. Phys. B: Condens. Matter **78**, 367 (1990).

[49] Y.-Y. Wang, G. F. Feng, T. E. Sutto, and Z. Shao, Phys. Rev. B **44**, 7098 (1991).

[50] C. Horie, Prog. Theor. Phys. **21**, 113 (1959).

[51] I. Egri, Solid State Commun. **44**, 563 (1982).

[52] K. Sturm, Adv. Phys. **31**, 1 (1982).

[53] I. Egri, J. Phys. C: Solid State Phys. **18**, 1191 (1985).

[54] Y. Y. Wang, S.C. Cheng, V. P. Dravid, and F. C. Zhang, Ultramicroscopy **59**, 109 (1995).

[55] R. Manzke, J. Phys. C **13**, 911 (1980).

[56] C. H. Chen, J. Silcox, and R. Vincent, Phys. Rev. B **12**, 64 (1975).

[57] Y. Liu, R. F. Willis, K. V. Emtsev, and T. Seyller, Phys. Rev. B **78**, 201403(R) (2008).

[58] M. Rocca, Surf. Sci. Rep. **22**, 1 (1995).

[59] T. Nagao, T. Hildebrandt, M. Henzler, and S. Hasegawa, Phys. Rev. Lett. **86**, 5747 (2001).

[60] R. Erni and N. D. Browning, Ultramicroscopy **108**, 84 (2008).

[61] K. A. Mkhoyan, T. Babinnec, S. E. Maccagnano, E. J. Kirkland, and J. Silcox, Ultramicroscopy **107**, 345 (2007).

[62] S. C. Cheng, Y. Y. Wang, and V. P. Dravid, Micron **27**, 167 (1996).

[63] D. S. Su and P. Schattschneider, Philos. Mag. A **65**, 1127 (1992).

[64] E. Kröger, Z. Phys. **216**, 115 (1968).

[65] J. P. R. Bolton and M. Chen, J. Phys.: Condens. Matter **7**, 3373 (1995).

[66] M. Couillard, A. Yurtsever, and D. A. Muller, Phys. Rev. B **77**, 085318 (2008).